Pattern formation of elastic waves and energy localization due to elastic gratings

A. Berezovski [a,*], J. Engelbrecht [a], M. Berezovski [b]

[a] *Institute of Cybernetics at Tallinn University of Technology, Akadeemia tee 21, Tallinn 12618, Estonia*
[b] *Embry-Riddle Aeronautical University, 600 S. Clyde Morris Boulevard, Daytona Beach, FL 32114, USA*

ARTICLE INFO

ABSTRACT

Elastic wave propagation through diffraction gratings is studied numerically in the plane strain setting. The interaction of the waves with periodically ordered elastic inclusions leads to a self-imaging Talbot effect for the wavelength equal or close to the grating size. The energy localization is observed at the vicinity of inclusions in the case of elastic gratings. Such a localization is absent in the case of rigid gratings.

© 2015 Elsevier Ltd. All rights reserved.

1. Introduction

Wave motion in solids is an extremely important physical phenomenon due to wide range of applications. The propagation of mechanical waves can be controlled via scattering induced by a material's structure. Given the high frequencies and high values of excitations used in contemporary technology, the material properties must be very clearly determined up to smaller scales and an internal structure of materials. The need to tailor materials able to meet various conditions is obvious. That is why during the last two decades, the attention to man-made metamaterials has been tremendously increased [41,20,27,44]. This is understandable because metamaterials are characterized by their properties beyond those of conventional engineering materials and therefore their practical applications display new qualities for technology. The reader is referred to more detailed overviews on this topic [34,35,25].

It is not surprising that the wave propagation in metamaterials cannot rely on classical continuum mechanics based on the homogeneity of materials. Indeed, the wave propagation in solids with inhomogeneities (inclusions) or microstructured solids at various scales has also been studied intensively based on various assumptions about the internal structure of the material [30,12,15] and various mathematical models were derived (see e.g. Engelbrecht and Berezovski [14]). From the physical viewpoint, the most important feature of waves in microstructured materials is the interaction of waves with inhomogeneities which is the source of wave dispersion, diffraction and interference. However, as in optics, one of the basic problems to be solved is the diffraction of waves on inhomogeneities. In light and atom optics, the diffraction of waves is a well-known and well-studied phenomenon, both for near-field (Fresnel diffraction) and far-field (Fraunhofer diffraction) zones. In solid mechanics the interest to the diffraction started due to the practical importance of the dynamic stress concentration on obstacles [31] and nondestructive testing [22]. The earlier theoretical studies related to the elastic wave diffraction on inclusions were shadowed by analytical difficulties [19,1]. It is remarkable, however, that the elastic counterpart of the well-known Talbot effect in optics [39] is not so largely studied. Discovered by Henry Fox Talbot in 1836, the phenomenon involves the diffraction of a plane wave through a grating. As a result of such a process, a regular diffraction structure, called the Talbot carpet, appears which reproduces the structure of the grating at multiples of a certain distance. This distance is now called the Talbot length. Lord Rayleigh [36] proved that the appearance of the Talbot structure was a consequence of the Fresnel diffraction. He also determined the Talbot length $z_T = 2a^2/\lambda$, where a is the period of the grating and λ is the wavelength of the incident periodic wave.

The interest to the Talbot effect, i.e. to the diffraction through a grating is recently increased due to novel possible applications of the physical phenomena related to the diffraction: for example, atom lithography [27], quantum and optical carpets [11], electron spin effect [40], effects of metallic gratings [38], phononic crystals [24,17], behavior of metamaterials [43], etc. Clearly the Talbot effect in solids needs more detailed analysis because this is a basic case of the

* Corresponding author.
  E-mail address: Arkadi.Berezovski@cs.ioc.ee (A. Berezovski).

diffraction phenomenon. The demonstration of the elastic Talbot effect [10] was performed in full analogy with optical case [26], i.e., under the Kirchhoff assumption that distances from the aperture are larger than wavelengths and the grating is rigid. However, it is practically impossible to implement a perfectly rigid grating into an elastic material. It is worth, therefore, to investigate wave patterns appearing in a more suitable elastic grating case. It is clear that following the theory of elasticity both the longitudinal and transverse waves must be taken into account in the diffraction pattern.

In spite of the linearity of governing equations of classical elasticity, it was possible to construct solutions to diffraction problems only for rather simple problems like, for example, the diffraction from a single rigid barrier in an elastic medium by using the Wiener–Hopf method [19], the interaction of an impact wave with a rigid circular disc [23] and the interaction of an impact wave with a rigid plane inclusion [33].

The situation is changed with the growth of computational power and the progress in numerical techniques. The development of finite difference [3], finite element [21], and finite volume [28] algorithms for wave propagation in solids resulted in the numerous applications to nondestructive testing [42,18,2]. An example of an effective numerical analysis is a study of the guided waves at a periodic array of coplanar slits using Bloch harmonics [17]. Design of new materials like phononic crystals [34] demands even more accurate prediction of the wave propagation in structured solids.

The advantage of numerical simulation is its generality, capable of predicting accurate wave fields for any composite with arbitrarily distributed scatterers. In the case of elastic wave propagation, the wave field can be simulated accurately by solving the elastodynamic equations for the matrix and the scatterers respectively. In what follows we present the results of numerical simulations of elastic wave propagation for simple geometry of substructure with different material properties. We limit ourselves by the plane strain case since it is sufficient to demonstrate basic effects. We do not apply any kind of homogenization; all computations are performed directly for given materials.

In Section 2 the numerical procedure is described briefly. The reference wave pattern due to the rigid grating is reviewed in Section 3. Section 4 is devoted to the results of numerical simulations of wave patterns due to the elastic grating. Transmittance and the influence of wavelength are analyzed in Sections 5 and 6, respectively. An unexpected result for the energy localization is reported in Section 7. Finally, in Section 8, conclusions are given stressing the emergence of wave patterns and the localization of energy. The governing equations and its dimensionless form are presented in Appendix A. The important problem of boundary conditions is explained in Appendix B.

2. Numerical procedure

The governing system of equations (see Appendix A) is solved numerically by means of the conservative finite-volume wave-propagation algorithm, which was proposed by LeVeque [28,29] and modified for the application to front propagation by Berezovski et al. [6], Berezovski and Maugin [8,9]. The algorithm was successfully applied for the wave propagation simulation in inhomogeneous solids [7].

The modification of the wave-propagation algorithm [9] is based on the non-equilibrium jump relations at the boundaries between computational cells. The main idea in the construction of the numerical algorithm is the consideration of every computational cell as a thermodynamic system [32]. Since we cannot expect that this thermodynamic system is in equilibrium, its local equilibrium state is described by averaged values of field quantities. The use of cell averages is a standard procedure in the finite-

volume methods. What is non-standard that is the introduction into consideration so-called "excess quantities" in the spirit of the thermodynamics of discrete systems [32].

Excess quantities represent the difference between values of true and averaged quantities [7]:

$$v_i = \overline{v}_i + V_i, \quad \sigma_{ij} = \overline{\sigma}_{ij} + \Sigma_{ij}. \tag{1}$$

Here v_i are components of the velocity vector, σ_{ij} are components of the stress tensor, overbars denote averaged quantities, and capital letters correspond to excess quantities.

Though excess quantities are determined formally everywhere inside computational cells, we need to know only their values at the boundaries of the cells, where they play the role of numerical fluxes that describe the interactions between neighboring cells [5]. These excess quantities are calculated by means of jump relations at the boundaries between cells [7]. It should be emphasized that jump relations used here provide the continuity of unknown fields at the boundaries between computational cells. The advantage of the algorithm is that every discontinuity in parameters is taken into account by the exact solution of the Riemann problem at each interface between discrete elements. The reflection and transmission of waves at each interface are handled automatically for any inhomogeneous media. The applied algorithm is conservative, stable up to the Courant number equal to 1, high-order accurate, and thermodynamically consistent [7,8].

3. Wave pattern due to rigid grating

As it was shown recently [10], the well-known Talbot effect in optics can be observed also in the case of elastic waves. The corresponding simulations, however, were performed for the case of perfectly rigid gratings. Here we demonstrate first a case where the size of rigid inclusions is equal to each other and to the distance between them. This scenario allows us to consider the problem independently from the length scales (see Appendix A). The geometry of the problem is shown in Fig. 1a. The grating is placed at 100 space steps from the left boundary.

The monochromatic plane wave is excited at the left boundary of the computational domain. The wavelength of the incident wave is equal to the size of the grating (20 space steps in the discretized computational domain). Boundary conditions at lateral boundaries are periodic (like Eqs. (47)–(48)). At the right boundary, the non-reflective boundary conditions (like Eqs. (45)–(46)) are applied. Note that in order to model rigid inclusions, all velocities and stresses are prescribed to be zero inside the inclusions. Additionally, boundary conditions for fixed boundary (similar to Eq. (B.4)) are prescribed at each side of the inclusion. Calculations performed up to 1400 time steps to avoid the influence of any reflection from the left boundary which is placed virtually at 500 space steps upstream the grating. It must be stressed that in this 2D elastic case both longitudinal and transverse wave exist.

The contour plots for the normal stress field along the longitudinal axis are shown in Fig. 1. The self-imaging Talbot carpet in the case of rigid grating is clearly seen in the contour plot (Fig. 1b). The emergent pattern is similar to this presented in [10]. The calculated pattern corresponds to the stress distribution at 1400 time steps. This case of rigid inclusions serves as the reference example for the comparison with the gratings composed by elastic scatterers.

4. Wave patterns due to elastic grating

The perfectly rigid grating is an idealization suited well for optics but hardly realized in solids. That is why we consider a more practical case with an elastic grating within an elastic matrix. To extend the
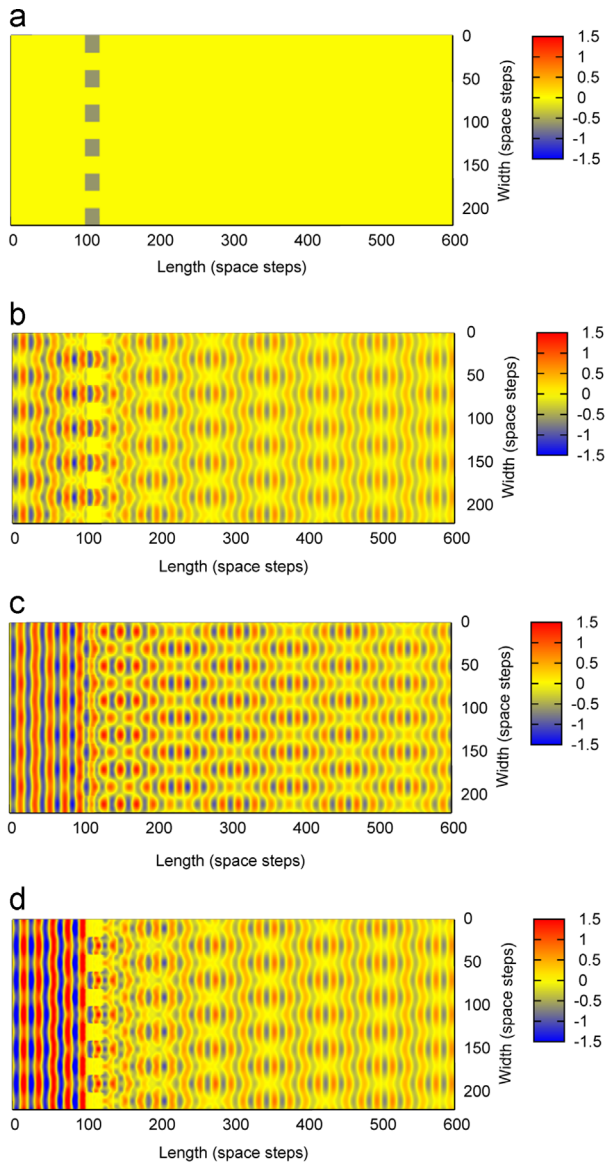
Fig. 1. Contour plots (Talbot carpets) of the normal stress field. (a) Geometry of the problem. (b) Talbot carpet for rigid inclusions at 1400 time steps. (c) Elastic case with low contrast materials. (d) Elastic case with high contrast materials.

results onto fully elastic case, we have chosen first the case when properties for the matrix material and the grating material differ considerably. Later this case is referred as high contrast materials.

4.1. High contrast materials

Namely, the properties of the carrier material $\rho = 8900$ kg/m^3, $c_p = 6040$ m/s, $c_s = 3000$ m/s correspond to a metal like Nickel, and grating properties correspond to those for Lucite: $\rho = 1100$ kg/m^3, $c_p = 2610$ m/s, $c_s = 1140$ m/s. The geometry of the problem remains the same as above, as well as loading and boundary conditions. As it was noted above (Section 2), the reflection and transmission of waves at each interface of an inclusion is handled automatically. As we can see in Fig. 1d, the appeared self-imaging wave pattern is very similar to that in the case of the rigid grating (Fig. 1b) because in both cases there is a big difference in the material properties.

4.2. Low contrast materials

To continue the investigation of the influence of the variation of material properties, we turn to the case where the properties for the
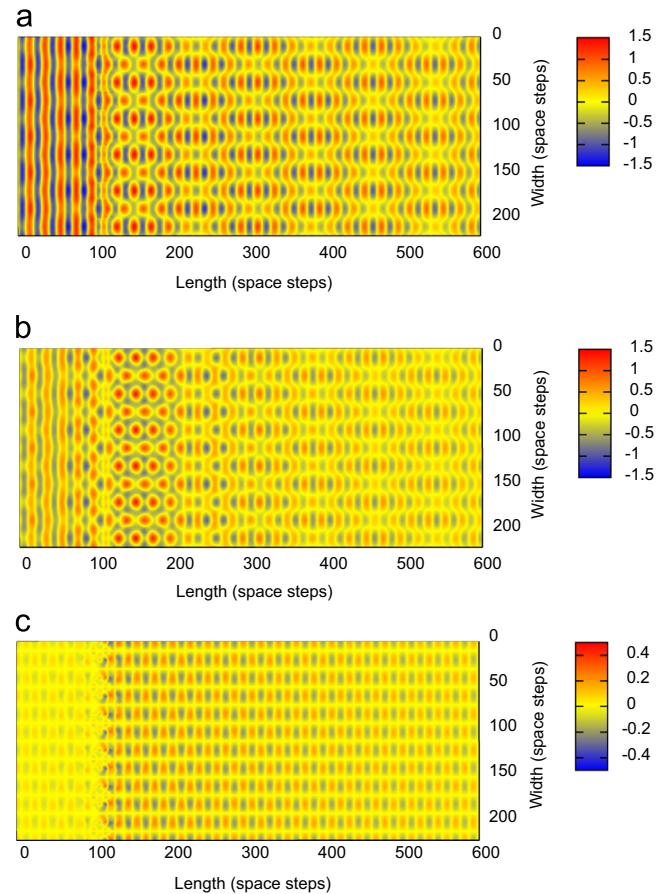

Fig. 2. Contour plots of the stress field. (a) Longitudinal normal stress. (b) Transverse normal stress. (c) Shear stress.

matrix material and the material of the grating do not differ considerably. This case is later referred as low contrast materials. Remaining the properties of the matrix material as in a metal like Nickel with $\rho = 8900$ kg/m^3, $c_p = 6040$ m/s, $c_s = 3000$ m/s, we choose the properties of grating material like those for zinc: $\rho = 7100$ kg/m^3, $c_p = 4210$ m/s, $c_s = 2440$ m/s. We still keep the geometry of the problem as above, as well as loading and boundary conditions. As a result, we obtain again a self-imaging wave pattern but with the different shape of formed wave packets (Fig. 1c). The difference in the distribution between normal stresses in longitudinal and transverse directions (and also shear stresses) is shown in Fig. 2. The normal stress in the transverse direction has maximum amplitudes immediately after the grating and further on a smaller, rather uniformly distributed pattern is generated. Shear stresses demonstrate uniform pattern everywhere downstream the grating.

4.3. Overall remarks

In general, self-imaging wave patterns appear in all cases but certain differences can be noticed. First, the main difference is seen in the near vicinity downstream the grating because the interference pattern is significantly influenced by the elasticity of inclusions. Later the patterns are slightly different but the cases with rigid and soft (high contrast) inclusions are more similar to each other than the case with low contrast materials.

The similarity in elastic wave propagation in the cases of rigid and very soft gratings is confirmed by the comparison of the normal stress distribution along the centerline shown in Fig. 3. Downstream the grating, the corresponding wave profiles are close to each other. At the same time, these profiles are essentially different from the wave
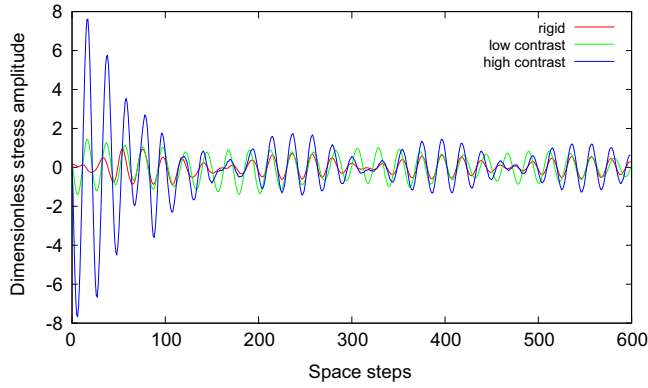
Fig. 3. Normal stress distribution along centerline due to diffraction grating.
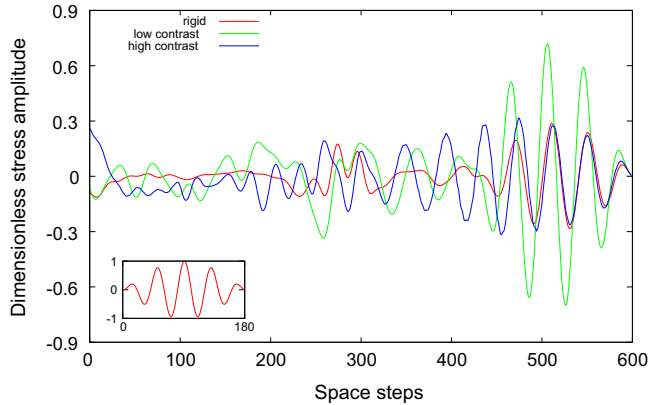

Fig. 4. Normal stress distribution along centerline for pulse loading. The box shows the shape of initial pulse.

profile for the low contrast in material properties of matrix and inclusions. It should be noted that the stress values are normalized by the initial normal stress amplitude. The grating is placed between 100 and 120 space steps.

5. Transmittance

The regular wave pattern emerges in the case of permanent (or long enough) monochromatic plane wave loading. This is again an idealized situation, which does not allow us to assess the transmittance properties of gratings. The transmittance can be observed for the finite pulse loading. For this purpose the finite pulse composed by two sinusoidal signals was generated at the left boundary. The attenuation of this signal determines the transmittance of a grating. The results of calculation of the normal stress distribution along centerline in the case of the pulse loading (Fig. 4) show that the transmittance in the case of high difference in material properties (both for rigid and soft inclusions) is about 0.3, whereas for the low difference in the properties it is much higher (0.7 for the considered case of Ni as matrix and Zn for inclusions). It is clear that the transmittance should be equal to one if the grating is made from the same material as the matrix. It should be noted that the transmittance cannot be reduced to the simple reflection and transmission coefficients due to the elastic interaction between scatterers and matrix.

6. Wavelength influence

Up to now the calculations were performed for the induced wavelength equal to the grating size. To demonstrate how the
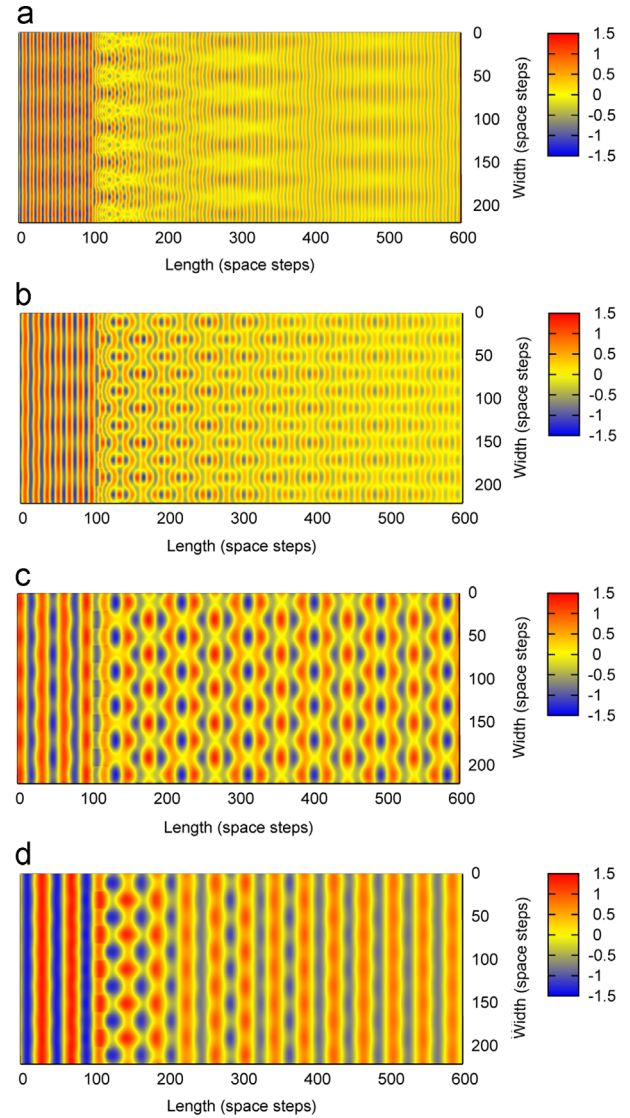

Fig. 5. Contour plots of the normal stress field for low contrast in material properties. (a) Wavelength is equal to 10 space steps. (b) Wavelength is equal to 15 space steps. (c) Wavelength is equal to 30 space steps. (d) Wavelength is equal to 40 space steps.

wavelength influences the wave pattern formation, results of calculations for four different wavelength are shown in Fig. 5. The geometry of the problem as well as boundary conditions is the same as above for low contrast materials.

As it is observed, the self-imaging wave pattern is almost lost for the wavelengths which are twice shorter (Fig. 5a) or twice longer (Fig. 5d) than the grating size. Nevertheless, the interference patterns demonstrate certain regularity. For wavelengths more closer to the grating size we see the emergence of the more clear patterns (Fig. 5b and c). However, these patterns differ significantly from the cases shown in Fig. 1 with the wavelength equal to grating size.

7. Energy localization

Besides the stress field, it is useful to know the distribution of the energy density. The strain energy density of an elastic isotropic material depends on the strain tensor as follows [37]:
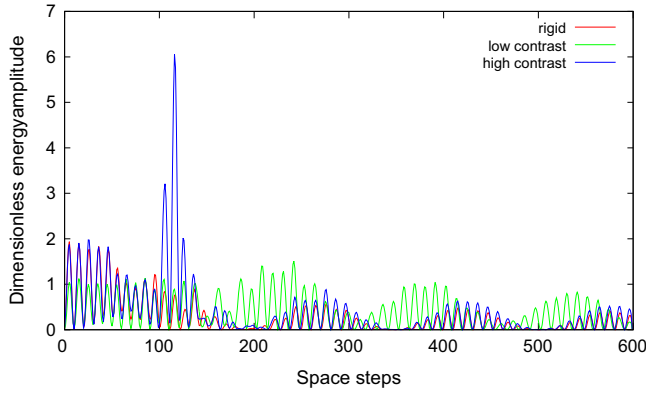
$$W = \tfrac{1}{2}(\sigma_{ij}\varepsilon_{ij}). \tag{2}$$
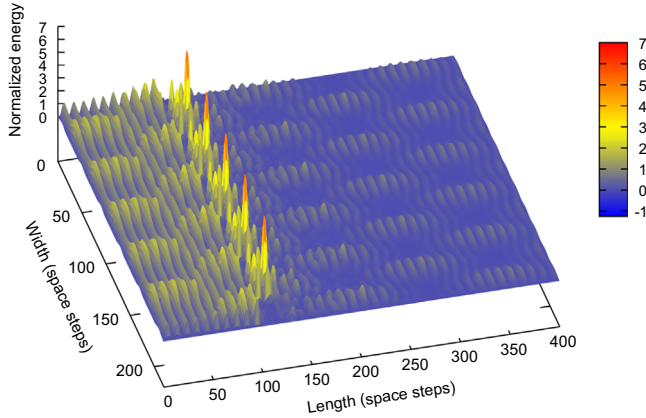
Fig. 6. Energy distribution along centerline.

Fig. 7. Overall energy distribution.

Fig. 8. Kinetic and elastic energy distribution along centerline for high contrast materials.

Fig. 9. Kinetic and elastic energy distribution along centerline for rigid inclusions. (Note the different scale from Fig. 8).

In the considered plane strain case $\varepsilon_{13} = \varepsilon_{23} = \varepsilon_{33} = 0$, and the expression for the strain energy density is reduced to

$$W = \tfrac{1}{2}(\sigma_{11}\varepsilon_{11} + \sigma_{22}\varepsilon_{22} + 2\sigma_{12}\varepsilon_{12}). \qquad (3)$$

The kinetic energy density is determined by velocities

$$K = \tfrac{1}{2}\rho(v_1^2 + v_2^2). \qquad (4)$$

The comparison of energy distribution $(W+K)$ along centerline for rigid, soft, and hard materials of inclusions is presented in Fig. 6. The distribution of energy downstream the grating for rigid and soft inclusions is very similar. However, there is a big difference between them in the neighborhood of the grating. The energy localization in the case of soft inclusions is induced by a big difference in the properties of the matrix material and the material of the grating and appears due to the elastic interaction between the matrix and scatterers. The overall energy distribution is shown in Fig. 7.

To analyze the energy localization in more detail, we calculated the kinetic and elastic energy separately in the case of high contrast materials (soft inclusions). The results of their distribution along centerline are presented in Fig. 8. It is clear that the kinetic energy is responsible for the energy localization due to high values of the particle velocity occurring immediately after the grating. One can observe that kinetic and elastic energies have an anti-phase synchronization upstream the grating, while downstream the grating they are synchronized in phase. The grating looks like an alternator of the synchronization for energy in elastic waves. The similar distribution of elastic and kinetic energy in the case of rigid inclusions is shown in Fig. 9. The comparison with the case of soft inclusions demonstrates that the change of the synchronization takes place in both cases, but there is no energy localization in the case of rigid inclusions.
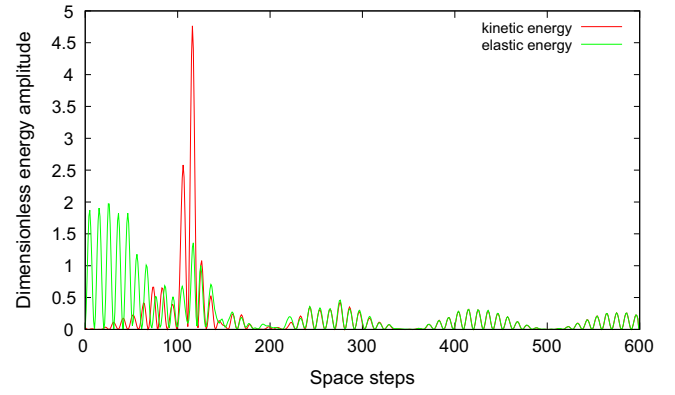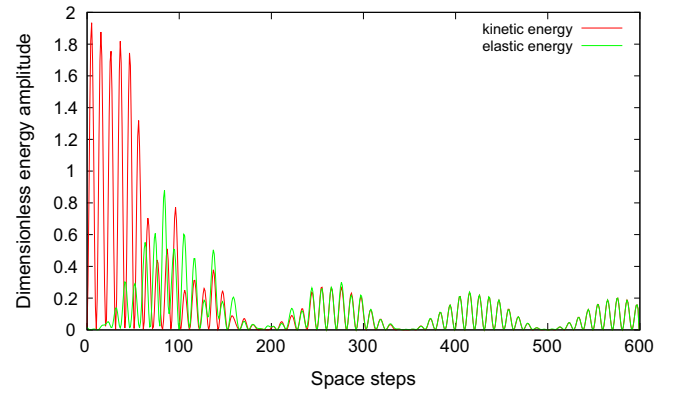
8. Conclusions

There are considerable mathematical difficulties in finding analytical solutions for elastic wave propagation in inhomogeneous elastic solids. An excellent overview on earlier results is given by Mow and Pao [31] which actually summarizes the efforts of analysis. Since then the possibilities of computational mechanics have been enormously increased. It is worth, therefore, to have efficient computational tools for the prediction of wave interactions with inhomogeneities. The applied version of the wave propagation algorithm is a robust, flexible, and efficient method for numerical experiments with the elastic wave propagation in inhomogeneous solids [7]. By means of this numerical method we are able to demonstrate the elastic Talbot effect which is characteristic for wave diffraction in optics [39].

Numerical simulations of the elastic wave diffraction on elastic gratings show both similarities and differences with the case of a rigid grating where waves are not transmitted through inclusions. The similarity is in the emergence of the self-imaging wave pattern for a narrow region of wavelengths close to the size of the grating. The variation of wave length (i.e. frequency) of the initial wave influences significantly the emerged pattern. For long waves the characteristic interference pattern is seen only at the close vicinity of the grating, while for the short waves the pattern is not formed at all. Variation of elastic properties of inclusions does not alter much the wave pattern but modifies the distribution of energy behind the grating.

The main difference from the case of the rigid grating is the energy localization in the middle of slits at the vicinity of inclusions in the case of high contrast materials (soft inclusions).

This unexpected result is due to a complicated interference and the influence of elasticity of the grating. At the same time, the overall self-imaging pattern in this case is very similar to the case of the rigid grating, whereas the low contrast materials exhibit significantly distinct wave patterns.

To demonstrate the influence of elastic properties of scatterers and matrix on the wave diffraction, we constrained ourselves by the simplest geometry with the normal loading direction. We did not impose any special boundary conditions at boundaries of inclusions. Surprisingly, even in this uncomplicated case the accounting of elasticity results in an unexpected energy localization. Certainly there are many more sophisticated cases where the variation in geometry and properties of scatterers and matrix, as well as in loading directions, may lead to an unusual behavior of waves (see e.g., [16,13]). Our goal was to attract the attention to inherent elastic effects.

Acknowledgments

Appendix A. Plane strain elasticity

Numerical simulation of elastic wave propagation is based on the solution of equations of elasticity. Neglecting both geometrical and physical nonlinearities, we can write the bulk equations of homogeneous linear isotropic elasticity in the absence of body force as follows [4]:

$$\rho_0 \frac{\partial v_i}{\partial t} = \frac{\partial \sigma_{ij}}{\partial x_j}, \tag{A.1}$$

$$\frac{\partial \sigma_{ij}}{\partial t} = \lambda \frac{\partial v_k}{\partial x_k} \delta_{ij} + \mu \left(\frac{\partial v_i}{\partial x_j} + \frac{\partial v_j}{\partial x_i} \right), \tag{A.2}$$

where t is time, x_j are spatial coordinates, v_i are components of the velocity vector, σ_{ij} is the Cauchy stress tensor, ρ_0 is the density, λ and μ are Lamé coefficients.

Consider a sample that is relatively thick along x_3, and where all applied forces are uniform in the x_3 direction. Since all derivatives with respect to x_3 vanish, all fields can be viewed as functions of x_1 and x_2 only. This situation is called plane strain. The corresponding displacement component (e.g., the component u_3 in the direction of x_3) vanishes and the others (u_1, u_2) are independent of that coordinate x_3; that is

$$u_3 = 0, \quad u_i = u_i(x_1, x_2), \quad i = 1, 2. \tag{A.3}$$

It follows that the strain tensor components, ε_{ij} are

$$\varepsilon_{i3} = 0, \quad \varepsilon_{ij} = \tfrac{1}{2}(u_{i,j} + u_{j,i}), \quad i,j = 1, 2. \tag{A.4}$$

The stress components follow then

$$\sigma_{3i} = 0, \quad \sigma_{33} = \frac{E}{1-2\nu} \left(\frac{\nu}{1+\nu} \varepsilon_{ii} \right), \quad i = 1, 2. \tag{A.5}$$

$$\sigma_{ij} = \frac{E}{1+\nu} \left(\varepsilon_{ij} + \frac{\nu}{1-2\nu} \varepsilon_{kk} \delta_{ij} \right), \quad i,j,k = 1, 2, \tag{A.6}$$

where E is Young's modulus, ν is Poisson's ratio, δ_{ij} is the unit tensor.

Inversion of Eq. (A.6) yields an expression for the strains in terms of stresses:

$$\varepsilon_{ij} = \frac{1+\nu}{E} (\sigma_{ij} - \nu \sigma_{kk} \delta_{ij}), \quad i,j,k = 1, 2. \tag{A.7}$$

System of Eqs. (A.1) and (A.2), specialized to plane strain conditions by Eqs. (A.3)–(A.7) has the form

$$\rho \frac{\partial v_1}{\partial t} = \frac{\partial \sigma_{11}}{\partial x} + \frac{\partial \sigma_{12}}{\partial y}, \tag{A.8}$$

$$\rho \frac{\partial v_2}{\partial t} = \frac{\partial \sigma_{21}}{\partial x} + \frac{\partial \sigma_{22}}{\partial y}. \tag{A.9}$$

Accordingly, compatibility conditions are represented as

$$\frac{\partial \varepsilon_{11}}{\partial t} = \frac{\partial v_1}{\partial x}, \tag{A.10}$$

$$\frac{\partial \varepsilon_{12}}{\partial t} = \frac{1}{2} \left(\frac{\partial v_1}{\partial y} + \frac{\partial v_2}{\partial x} \right), \tag{A.11}$$

$$\frac{\partial \varepsilon_{22}}{\partial t} = \frac{\partial v_2}{\partial y}. \tag{A.12}$$

Stress–strain relations (Hooke's law) close the system of governing equations

$$\sigma_{11} = (\lambda + 2\mu)\varepsilon_{11} + \lambda \varepsilon_{22}, \tag{A.13}$$

$$\sigma_{12} = \sigma_{21} = 2\mu \varepsilon_{12}, \tag{A.14}$$

$$\sigma_{22} = (\lambda + 2\mu)\varepsilon_{22} + \lambda \varepsilon_{11}. \tag{A.15}$$

Time derivatives of stress–strain relations together with compatibility conditions determine

$$\frac{\partial \sigma_{11}}{\partial t} = (\lambda + 2\mu) \frac{\partial v_1}{\partial x} + \lambda \frac{\partial v_2}{\partial y}, \tag{A.16}$$

$$\frac{\partial \sigma_{22}}{\partial t} = \lambda \frac{\partial v_1}{\partial x} + (\lambda + 2\mu) \frac{\partial v_2}{\partial y}, \tag{A.17}$$

$$\frac{\partial \sigma_{12}}{\partial t} = \frac{\partial \sigma_{21}}{\partial t} = \mu \left(\frac{\partial v_1}{\partial y} + \frac{\partial v_2}{\partial x} \right). \tag{A.18}$$

These equations together with the balance of linear momentum (A.8) and (A.9) form the system of equations, which is convenient for a numerical solution.

A.1. Dimensionless variables

In the grating problem we have three independent space scales:

- the individual slit size a,
- the width of the plate (slit thickness) w,
- the wavelength L.

The time scale of the problem is determined by means of the longitudinal wave speed c_p and the reference wavelength L as follows:

$$t_0 = \frac{L}{c_p}. \tag{A.19}$$

Introducing dimensionless variables

$$X = \frac{x}{a}, \quad Y = \frac{y}{w}, \quad T = \frac{t}{t_0} = \frac{t c_p}{L}, \tag{A.20}$$

and dimensionless unknowns

$$V_i = \frac{v_i}{c_p}, \quad \Sigma_{ij} = \frac{\sigma_{ij}}{\sigma_0}, \tag{A.21}$$

we can re-write the governing equations in the form

$$\frac{\rho c_p^2}{L} \frac{\partial V_1}{\partial T} = \frac{\sigma_0}{a} \frac{\partial \Sigma_{11}}{\partial X} + \frac{\sigma_0}{w} \frac{\partial \Sigma_{12}}{\partial Y}, \tag{A.22}$$

$$\frac{\rho c_p^2}{L}\frac{\partial V_2}{\partial T}=\frac{\sigma_0}{a}\frac{\partial \Sigma_{21}}{\partial X}+\frac{\sigma_0}{w}\frac{\partial \Sigma_{22}}{\partial Y}. \tag{A.23}$$

$$\frac{\sigma_0 c_p}{L}\frac{\partial \Sigma_{11}}{\partial T}=\frac{(\lambda+2\mu)c_p}{a}\frac{\partial V_1}{\partial X}+\frac{\lambda c_p}{w}\frac{\partial V_2}{\partial Y}, \tag{A.24}$$

$$\frac{\sigma_0 c_p}{L}\frac{\partial \Sigma_{22}}{\partial T}=\frac{\lambda c_p}{a}\frac{\partial V_1}{\partial X}+\frac{(\lambda+2\mu)c_p}{w}\frac{\partial V_2}{\partial Y}, \tag{A.25}$$

$$\frac{\sigma_0 c_p}{L}\frac{\partial \Sigma_{12}}{\partial T}=\frac{\sigma_0 c_p}{L}\frac{\partial \Sigma_{21}}{\partial T}=\frac{\mu c_p}{w}\frac{\partial V_1}{\partial Y}+\frac{\mu c_p}{a}\frac{\partial V_2}{\partial X}. \tag{A.26}$$

The natural choice of the scale for stresses follows from Eqs. (26) to (27)

$$\sigma_0 = \rho c_p^2 = \lambda + 2\mu. \tag{A.27}$$

Such a choice of the characteristic stress σ_0 reduces the governing equations to

$$\frac{1}{L}\frac{\partial V_1}{\partial T}=\frac{1}{a}\frac{\partial \Sigma_{11}}{\partial X}+\frac{1}{w}\frac{\partial \Sigma_{12}}{\partial Y}, \tag{A.28}$$

$$\frac{1}{L}\frac{\partial V_2}{\partial T}=\frac{1}{a}\frac{\partial \Sigma_{21}}{\partial X}+\frac{1}{w}\frac{\partial \Sigma_{22}}{\partial Y}. \tag{A.29}$$

$$\frac{1}{L}\frac{\partial \Sigma_{11}}{\partial T}=\frac{1}{a}\frac{\partial V_1}{\partial X}+\frac{\lambda}{w(\lambda+2\mu)}\frac{\partial V_2}{\partial Y}, \tag{A.30}$$

$$\frac{1}{L}\frac{\partial \Sigma_{22}}{\partial T}=\frac{\lambda}{a(\lambda+2\mu)}\frac{\partial V_1}{\partial X}+\frac{1}{w}\frac{\partial V_2}{\partial Y}, \tag{A.31}$$

$$\frac{1}{L}\frac{\partial \Sigma_{12}}{\partial T}=\frac{1}{L}\frac{\partial \Sigma_{21}}{\partial T}=\frac{\mu}{w(\lambda+2\mu)}\frac{\partial V_1}{\partial Y}+\frac{\mu}{a(\lambda+2\mu)}\frac{\partial V_2}{\partial X}. \tag{A.32}$$

As one can see, there exists the specific case characterizing by the equality of all scales ($L=a=w$), where the wavefields depend on material properties only. This distinguished case is used as the main example in numerical simulations of the interaction of elastic waves with an elastic grating.

Appendix B. Boundary conditions

Boundaries in solid mechanics can be classified as (without external loading)

1. fixed boundary, i.e. velocities at the boundary are zero;
2. free boundary, i.e. no stresses acting at the boundary;
3. non-reflective boundary, which means the absence of any reflection.

Additionally, periodic boundary conditions may be also imposed.

B.1. Left boundary

Considering the left boundary as an example, we expect that the state of cells adjacent to the left boundary is known (at least partly). For the proper computations, we need to know as many values of averaged quantities in advance as possible.

It should be noted that Riemann invariants along left-moving characteristic line should be conserved here independently of the kind of the boundary, so that

$$(\overline{\sigma}_{11})_{0m}+(\rho c_p)_{0m}(\overline{v}_1)_{0m}=(\overline{\sigma}_{11})_{1m}+(\rho c_p)_{1m}(\overline{v}_1)_{1m}, \tag{B.1}$$

$$(\overline{\sigma}_{21})_{0m}+(\rho c_s)_{0m}(\overline{v}_2)_{0m}=(\overline{\sigma}_{21})_{1m}+(\rho c_s)_{1m}(\overline{v}_2)_{1m}. \tag{B.2}$$

The conservation of Riemann invariants allows us to determine additionally the values of average stresses explicitly.

B.1.1. Left boundary—fixed
In the case of the fixed left boundary, averaged velocities should be zero

$$(\overline{v}_1)_{0m}=0, \quad (\overline{v}_2)_{0m}=0. \tag{B.3}$$

It follows from Eqs. (A.33)–(A.34) that

$$(\overline{\sigma}_{11})_{0m}=(\overline{\sigma}_{11})_{1m}+(\rho c_p)_{1m}(\overline{v}_1)_{1m}, \quad (\overline{\sigma}_{21})_{0m}=(\overline{\sigma}_{21})_{1m}+(\rho c_s)_{1m}(\overline{v}_2)_{1m}. \tag{B.4}$$

B.1.2. Left boundary—free
The absence of stresses at the free boundary means

$$(\overline{\sigma}_{11})_{0m}=0, \quad (\overline{\sigma}_{21})_{0m}=0, \quad (\overline{\sigma}_{22})_{0m}=0. \tag{B.5}$$

Accordingly, average velocities are computed by means of Eqs. (A.33) and (A.34)

$$(\overline{\sigma}_{11})_{1m}+(\rho c_p)_{1m}(\overline{v}_1)_{1m}=(\rho c_p)_{0m}(\overline{v}_1)_{0m}, \tag{B.6}$$

$$(\overline{\sigma}_{21})_{1m}+(\rho c_s)_{1m}(\overline{v}_2)_{1m}=(\rho c_s)_{0m}(\overline{v}_2)_{0m}. \tag{B.7}$$

B.1.3. Left boundary—non-reflective
In the non-reflective case, we expect that the Riemann invariants along characteristic lines incoming from boundary cells should be zero:

$$(\overline{\sigma}_{11})_{0m}-(\rho c_p)_{0m}(\overline{v}_1)_{0m}=0, \quad (\overline{\sigma}_{21})_{0m}-(\rho c_s)_{0m}(\overline{v}_2)_{0m}=0. \tag{B.8}$$

Together with the conservation of Riemann invariants (A.33) and (A.34) they form the system of equations for the determination of values of averaged velocities and stresses. The solution is the following:

$$2(\overline{\sigma}_{11})_{0m}=2(\rho c_p)_{0m}(\overline{v}_1)_{0m}=(\overline{\sigma}_{11})_{1m}+(\rho c_p)_{1m}(\overline{v}_1)_{1m}, \tag{B.9}$$

$$2(\overline{\sigma}_{21})_{0m}=2(\rho c_s)_{0m}(\overline{v}_2)_{0m}=(\overline{\sigma}_{21})_{1m}+(\rho c_s)_{1m}(\overline{v}_2)_{1m}. \tag{B.10}$$

B.1.4. Left boundary—periodic
Considering periodic boundary conditions we suggest that the state of cells at the left boundary is the same as the state of cells adjacent to the right boundary

$$(\overline{v}_1)_{0m}=(\overline{v}_1)_{nn-2m}, \quad (\overline{v}_2)_{0m}=(\overline{v}_2)_{nn-2m}, \tag{B.11}$$

$$(\overline{\sigma}_{11})_{0m}=(\overline{\sigma}_{11})_{nn-2m}, \quad (\overline{\sigma}_{21})_{0m}=(\overline{\sigma}_{21})_{nn-2m}. \tag{B.12}$$

B.1.5. Left boundary—loading
External loading can be represented as a time-dependent state of boundary cells. The general form of loading condition for horizontal components of velocity and stress tensor

$$A(\overline{\sigma}_{11})_{0m}+B(\overline{v}_1)_{0m}=f(t), \tag{B.13}$$

together with the conservation of the corresponding Riemann invariant

$$(\overline{\sigma}_{11})_{1m}+(\rho c_p)_{1m}(\overline{v}_1)_{0m}=(\overline{\sigma}_{11})_{0m}+(\rho c_p)_{0m}(\overline{v}_1)_{0m}, \tag{B.14}$$

forms the linear system of equations for the determination of values $(\overline{\sigma}_{11})_{0m}$ and $(\overline{v}_1)_{0m}$. For example, if only stress is prescribed

$$(\overline{\sigma}_{11})_{0m}=f(t), \tag{B.15}$$

then the corresponding velocity satisfies

$$(\overline{\sigma}_{11})_{1m}+(\rho c_p)_{1m}(\overline{v}_1)_{1m}=f(t)+(\rho c_p)_{0m}(\overline{v}_1)_{0m}. \tag{B.16}$$

For shear components we have, similarly, the system of equations

$$C(\overline{\sigma}_{21})_{0m}+D(\overline{v}_2)_{0m}=g(t), \tag{B.17}$$

$$(\overline{\sigma}_{21})_{1m}+(\rho c_s)_{1m}(\overline{v}_2)_{1m}=(\overline{\sigma}_{21})_{0m}+(\rho c_s)_{0m}(\overline{v}_2)_{0m}, \tag{B.18}$$

which determine the values of $(\overline{\sigma}_{21})_{0m}$ and $(\overline{v}_2)_{0m}$.

For other boundaries the boundary conditions are determined similarly. These boundary conditions are used at every corresponding boundary by the performing of calculations.

References

[1] Achenbach J. Wave Propagation in elastic solids. Amsterdam: Elsevier; 1984.
[2] Aggelis DG. Wave propagation through engineering materials; assessment and monitoring of structures through non-destructive techniques. Mater Struct 2013;46:519–32.
[3] Appelö D, Petersson NA. A stable finite difference method for the elastic wave equation on complex geometries with free surfaces. Commun Comput Phys 2009;5:84–107.
[4] Barber JR. Elasticity. Dordrecht: Springer; 2009.
[5] Berezovski A. Thermodynamic interpretation of finite volume algorithms. J Struct Mech (Raken Mek) 2011;44:3–156.
[6] Berezovski A, Engelbrecht J, Maugin G. Thermoelastic wave propagation in inhomogeneous media. Arch Appl Mech 2000;70:694–706.
[7] Berezovski A, Engelbrecht J, Maugin GA. Numerical simulation of waves and fronts in inhomogeneous solids. Singapore: World Scientific; 2008.
[8] Berezovski A, Maugin G. Simulation of thermoelastic wave propagation by means of a composite wave-propagation algorithm. J. Comput. Phys. 2001;168:249–64.
[9] Berezovski A, Maugin GA. Thermoelastic wave and front propagation. J Thermal Stress 2002;25:719–43.
[10] Berezovski A, Tang W-X, Wan W. Elastic wave Talbot effect in solids with inclusions. Mech Res Commun 2014;60:21–6.
[11] Berry M, Marzoli I, Schleich W. Quantum carpets, carpets of light. Phys World 2001;14:39–44.
[12] Capriz G. Continua with microstructure. New York: Springer-Verlag; 1989.
[13] Colquitt D, Craster R, Antonakakis T, Guenneau S. Rayleigh–Bloch waves along elastic diffraction gratings. Proc R Soc Lond A: Math Phys Eng Sci 2015; 471: 20140465.
[14] Engelbrecht J, Berezovski A. Reflections on mathematical models of deformation waves in elastic microstructured solids. Math Mech Compl Syst 2015;3:43–82.
[15] Eringen AC. Microcontinuum field theories. New York: Springer; 1999.
[16] Every A. Guided elastic waves at a periodic array of thin coplanar cavities in a solid. Phys Rev B 2008;78:174104.
[17] Every A, Maznev A. Guided elastic waves at periodically structured surfaces and interfaces. In: IUTAM symposium on recent advances of acoustic waves in solids. Amsterdam: Springer; 2010. p. 107–17.
[18] Ginzel E. NDT modelling: an overview. In: Proceedings of conference on modelling in non-destructive testing, Pretoria, South Africa; 2007.
[19] Graff KF. Wave motion in elastic solids. New York: Dover Publications; 1975.
[20] Guenneau S, Movchan A, Pétursson G, Ramakrishna SA. Acoustic metamaterials for sound focusing and confinement. New J Phys 2007;9:399.
[21] Ham S, Bathe K-J. A finite element method enriched for wave propagation problems. Comput Struct 2012;94:1–12.
[22] Hellier C, Hellier C. Handbook of nondestructive evaluation, vol. 10. New York: McGraw-Hill; 2001.
[23] Hirose S, Achenbach J. BEM method to analyze the interaction of an acoustic pulse with a rigid circular disk. Wave Motion 1988;10:267–75.
[24] Hou Z, Assouar BM. Band gap in phononic crystal thin plate with/without mirror plane. In: IUTAM symposium on recent advances of acoustic waves in solids. Amsterdam: Springer; 2010. p. 325-31.
[25] Hussein MI, Leamy MJ, Ruzzene M. Dynamics of phononic Mater Struct: historical origins, recent progress, and future outlook. Appl Mech Rev 2014;66:040802.
[26] Knopoff L. Diffraction of elastic waves. J Acoust Soc Am 1956;28:217–29.
[27] Lee J-H, Singer JP, Thomas EL. Micro-/nanostructured mechanical metamaterials. Adv Mater 2012;24:4782–810.
[28] LeVeque RJ. Wave propagation algorithms for multidimensional hyperbolic systems. J Comput Phys 1997;131:327–53.
[29] LeVeque RJ. Finite volume methods for hyperbolic problems. Cambridge, UK: Cambridge University Press; 2002.
[30] Mindlin R. Micro-structure in linear elasticity. Arch Ration Mech Anal 1964;16:51–78.
[31] Mow C-C, Pao Y-H. The diffraction of elastic waves and dynamic stress concentrations. Technical report R-482-PR, Rand Corporation Santa Monica, CA; 1971.
[32] Muschik W, Berezovski A. Thermodynamic interaction between two discrete systems in non-equilibrium. J Non-Equilib Thermodyn 2004;29:237–55.
[33] Mykhaskiv V. Transient response of a plane rigid inclusion to an incident wave in an elastic solid. Wave Motion 2005;41:133–44.
[34] Pennec Y, Vasseur JO, Djafari-Rouhani B, Dobrzyński L, Deymier PA. Two-dimensional phononic crystals: examples and applications. Surf Sci Rep 2010;65:229–91.
[35] Radousky HB, Liang H. Energy harvesting: an integrated view of materials, devices and applications. Nanotechnology 2012;23:502001.
[36] Rayleigh L. On copying diffraction-gratings, and on some phenomena connected therewith. Lond Edinb Dublin Philos Mag J Sci 1881;11:196–205.
[37] Sadd MH. Elasticity: theory applications, and numerics. Amsterdam: Academic Press; 2009.
[38] Sanchez-Brea LM, Torcal-Milla FJ, Bernabeu E. Talbot effect in metallic gratings under Gaussian illumination. Opt Commun 2007;278:23–7.
[39] Talbot HF. Facts relating to optical science. Lond Edinb Philos Mag J Sci 1836;9:401–7.
[40] Tang W-X, Paganin D, Wan W. Proposal for electron quantum spin Talbot effect. Phys Rev B 2012;85:064418.
[41] Torquato S. Modeling of physical properties of composite materials. Int J Solids Struct 2000;37:411–22.
[42] Wu T-T. Elastic wave propagation and nondestructive evaluation of materials. Proc Natl Sci Counc Rep China—Part A: Phys Sci Eng 1999; 23: 703–15.
[43] Zhao W, Huang X, Lu Z. Super Talbot effect in indefinite metamaterial. Opt Exp 2011;19:15297–303.
[44] Zheng X, Lee H, Weisgraber TH, Shusteff M, Deotte JR, Duoss E, et al. Ultralight, ultra-stiff mechanical metamaterials. Science 2014;344:1373–6.